

ACCEPTED MANUSCRIPT • OPEN ACCESS

## Neural decoding of electrocorticographic signals using dynamic mode decomposition

To cite this article before publication: Yoshiyuki Shiraishi *et al* 2020 *J. Neural Eng.* in press <https://doi.org/10.1088/1741-2552/ab8910>

### Manuscript version: Accepted Manuscript

Accepted Manuscript is “the version of the article accepted for publication including all changes made as a result of the peer review process, and which may also include the addition to the article by IOP Publishing of a header, an article ID, a cover sheet and/or an ‘Accepted Manuscript’ watermark, but excluding any other editing, typesetting or other changes made by IOP Publishing and/or its licensors”

This Accepted Manuscript is © 2020 The Author(s). Published by IOP Publishing Ltd..

As the Version of Record of this article is going to be / has been published on a gold open access basis under a CC BY 3.0 licence, this Accepted Manuscript is available for reuse under a CC BY 3.0 licence immediately.

Everyone is permitted to use all or part of the original content in this article, provided that they adhere to all the terms of the licence <https://creativecommons.org/licenses/by/3.0>

Although reasonable endeavours have been taken to obtain all necessary permissions from third parties to include their copyrighted content within this article, their full citation and copyright line may not be present in this Accepted Manuscript version. Before using any content from this article, please refer to the Version of Record on IOPscience once published for full citation and copyright details, as permissions may be required. All third party content is fully copyright protected and is not published on a gold open access basis under a CC BY licence, unless that is specifically stated in the figure caption in the Version of Record.

View the [article online](#) for updates and enhancements.

1    For ***Journal of Neural Engineering***

2  
3    **Neural decoding of electrocorticographic signals using dynamic mode**

4    **decomposition**

5  
6    Yoshiyuki Shiraishi<sup>a</sup>, Yoshinobu Kawahara<sup>b,c</sup>, Okito Yamashita<sup>b,d</sup>, Ryohei Fukuma<sup>a,e</sup>,

7    Shota Yamamoto<sup>e</sup>, Youichi Saitoh<sup>e,f</sup>, Haruhiko Kishima<sup>e</sup>, Takafumi Yanagisawa<sup>a,e,g</sup>

8  
9    <sup>a</sup> Osaka University, Institute for Advanced Co-Creation Studies, 2-2 Yamadaoka, Suita,  
10      Osaka 565-0871, Japan

11    <sup>b</sup> RIKEN Center for Advanced Intelligence Project, Nihonbashi 1-chome Mitsui  
12      Building, 15th floor, 1-4-1 Nihonbashi, Chuo-ku, Tokyo 103-0027, Japan

13    <sup>c</sup> Institute of Mathematics for Industry, Kyushu University, 744 Motooka, Nishi-ku,  
14      Fukuoka 819-0395, Japan

15    <sup>d</sup> ATR Neural Information Analysis Laboratories, Department of Computational Brain  
16      Imaging, 2-2-2 Hikaridai, Seika-cho, Kyoto 619-0288, Japan

17    <sup>e</sup> Osaka University Graduate School of Medicine, Department of Neurosurgery, 2-2  
18      Yamadaoka, Suita, Osaka 565-0871, Japan

1  
2  
3  
4  
5 19 <sup>f</sup>Osaka University Graduate School of Medicine, Department of Neuromodulation and  
6  
7  
8 20 Neurosurgery, 2-2 Yamadaoka, Suita, Osaka 565-0871, Japan  
9  
10  
11 21 <sup>g</sup>ATR Computational Neuroscience Laboratories, Department of Neuroinformatics, 2-2-  
12  
13  
14 22 2 Hikaridai, Seika-cho, Kyoto 619-0288, Japan  
15  
16  
17  
18  
19  
20 24 **Corresponding author:** Takufumi Yanagisawa, Osaka University, Institute for  
21  
22  
23 25 Advanced Co-Creation Studies, 2-2 Yamadaoka, Suita, Osaka 565-0871, Japan  
24  
25  
26 26 Tel.: +81-66-879-3652  
27  
28 27 Fax: +81-66-879-3659  
29  
30  
31  
32 28 tyanagisawa@nsurg.med.osaka-u.ac.jp  
33  
34  
35  
36  
37  
38  
39  
40  
41  
42  
43  
44  
45  
46  
47  
48  
49  
50  
51  
52  
53  
54  
55  
56  
57  
58  
59  
60

Accepted Manuscript

1  
2  
3  
4  
5     30   **Abstract**

6  
7  
8     31   *Objective.* Brain-computer interfaces (BCIs) using electrocorticographic (ECoG) signals  
9  
10    32   have been developed to restore the communication function of severely paralyzed  
11  
12    33   patients. However, the limited amount of information derived from ECoG signals  
13  
14    34   hinders their clinical applications. We aimed to develop a method to decode ECoG  
15  
16    35   signals using spatiotemporal patterns characterizing movement types to increase the  
17  
18    36   amount of information gained from these signals. *Approach.* Previous studies have  
19  
20    37   demonstrated that motor information could be decoded using powers of specific  
21  
22    38   frequency bands of the ECoG signals estimated by fast Fourier transform (FFT) or  
23  
24    39   wavelet analysis. However, because FFT is evaluated for each channel, the temporal and  
25  
26    40   spatial patterns among channels are difficult to evaluate. Here, we used dynamic mode  
27  
28    41   decomposition (DMD) to evaluate the spatiotemporal pattern of ECoG signals and  
29  
30    42   evaluated the accuracy of motor decoding with the DMD modes. We used ECoG signals  
31  
32    43   during three types of hand movements, which were recorded from 11 patients implanted  
33  
34    44   with subdural electrodes. From the signals at the time of the movements, the modes and  
35  
36    45   powers were evaluated by DMD and FFT and were decoded using support vector  
37  
38    46   machine. We used the Grassmann kernel to evaluate the distance between modes  
39  
40    47   estimated by DMD (DMD mode). In addition, we decoded the DMD modes, in which

1  
2  
3  
4  
5     48 the phase components were shuffled, to compare the classification accuracy. *Main*  
6  
7     49 *results*. The decoding accuracy using DMD modes was significantly better than that  
8  
9     50 using FFT powers. The accuracy significantly decreased when the phases of the DMD  
10  
11 mode were shuffled. Among the frequency bands, the DMD mode at approximately 100  
12  
13 Hz demonstrated the highest classification accuracy. *Significance*. DMD successfully  
14  
15 captured the spatiotemporal patterns characterizing the movement types and contributed  
16  
17 to improving the decoding accuracy. This method can be applied to improve BCIs to  
18  
19 help severely paralyzed patients communicate.

20  
21  
22  
23  
24  
25  
26  
27  
28  
29  
30  
31  
32     56

33  
34     57 **Keywords:** Dynamic mode decomposition, electrocorticography, neural decoding,  
35  
36     58 Grassmann kernel, principal angle

37  
38  
39  
40  
41  
42  
43  
44  
45  
46  
47  
48  
49  
50  
51  
52  
53  
54  
55  
56  
57  
58  
59  
60

1  
2  
3  
4  
5     61   **1. Introduction**

6  
7  
8     62   A brain–computer interface (BCI), which enables communication via brain activity, is  
9  
10     63   the only way to express thoughts for severely paralyzed patients who are completely  
11  
12     64   unable to move their body [1]. BCIs are in high demand for these patients [2], who  
13  
14     65   choose to undergo invasive procedures involving the placement of electrodes on the  
15  
16     66   surface [3] or inside the cortex [4, 5]. An electrocorticographic (ECoG) signal, which is  
17  
18     67   measured by a surface electrode, is a promising signal for use in BCIs [6] due to its  
19  
20     68   stability [7] and less invasive nature compared to penetrating electrodes [8, 9]. An  
21  
22     69   ECoG-BCI was successfully applied to a severely paralyzed patient with amyotrophic  
23  
24     70   lateral sclerosis (ALS) and enabled the patient to stably communicate for months [10].  
25  
26     71   However, much less information is derived from an ECoG signal than from penetrating  
27  
28     72   electrodes [11]. The patient with ALS was able to type faster using unit activity  
29  
30     73   recorded by a penetrating electrode, at more than 30 characters per minute [11], than  
31  
32     74   using ECoG signals [10]. Thus, for the clinical application of ECoG-BCIs, some novel  
33  
34     75   technologies to extract information from ECoG signals are necessary.

35  
36  
37  
38  
39  
40  
41  
42  
43  
44  
45  
46  
47  
48  
49  
50     76   To decode the ECoG signals, the oscillation component is considered to have  
51  
52  
53     77   important information, and various power spectral density (PSD) estimations [12-14]  
54  
55  
56  
57     78   have been used as features for machine learning [15-19]. Among the methods to

1  
2  
3  
4  
5 79 evaluate the PSD [18], fast Fourier transform (FFT) is often used for online decoding  
6  
7  
8 80 because of the low calculation cost [20]. FFT evaluates the powers of some frequency  
9  
10 bands for each channel in a time series and for individual time points in space.  
11  
12  
13 82 However, because these features are independently evaluated, FFT cannot evaluate the  
14  
15 patterns of ECoG signals in both space and time simultaneously. Therefore, a method to  
16  
17  
18 84 characterize the nonlinear dynamics as the linear summation of coherent patterns across  
19  
20  
21 85 both space and time (e.g., frequency and phase) is necessary.

22  
23  
24  
25  
26 86 Dynamic mode decomposition (DMD) has recently attracted attention as a way of  
27  
28  
29 87 obtaining modal representations of nonlinear dynamics from general multivariate time  
30  
31  
32 88 series data without explicit prior knowledge about the dynamics [21, 22]. DMD is  
33  
34  
35 89 closely related to spectral analysis of the Koopman operator (see Supplemental  
36  
37  
38 90 Information) and has been successfully applied for the extraction of spatiotemporal  
39  
40  
41 91 patterns, broadly in fluid mechanics [21-24], but rarely in neuroscience, e.g., ECoG and  
42  
43  
44 92 functional magnetic resonance imaging (fMRI) [25-28]. Although a previous study  
45  
46  
47 93 using human ECoG signals demonstrated that the DMD was able to capture some  
48  
49  
50 94 characteristic spatiotemporal patterns related to spindles [27], the spatiotemporal  
51  
52  
53 95 patterns were not used for neural decoding. It has not been revealed whether the spatial  
54  
55  
56 96 and temporal coherent patterns identified by DMD improve the accuracy of the neural

1  
2  
3  
4  
5 97 decoding used in BCI technology.  
6  
7

8 98 A problem in the application of DMD for neural decoding is that DMD transforms  
9  
10 99 the spatial and temporal signals into a set of vectors representing the characteristic  
11  
12 100 spatial mode, which has a characteristic frequency in the time domain. Notably, because  
13  
14 101 the characteristic frequency of the DMD mode is estimated from single trial data, the frequency  
15  
16 102 is not fixed across trials and varies depending on the original signals. Therefore, to classify  
17  
18 103 the signals by the vectors estimated by DMD, proper metrics are needed to evaluate  
19  
20 104 how the sets of vectors are similar among trials. Here, we used the principal angle as a  
21  
22 105 metric to evaluate the relationship among the sets of vectors for each trial [29]. A  
23  
24 106 Grassmann kernel was used with support vector machine (SVM) to classify the set of  
25  
26 107 vectors. In this study, we classified upper limb movements using the DMD components  
27  
28 108 with SVM. The classification accuracy using the DMD component was compared with  
29  
30 109 that using the FFT powers and that using the DMD components whose phases were  
31  
32 110 shuffled.

33 111

34 112 **2. Methods**

35 113 **2.1. Subjects**

36 114 Eleven patients (4 females, 7 males; age range, 13–66 years) with subdural electrodes  
37  
38  
39  
40  
41  
42  
43  
44  
45  
46  
47  
48  
49  
50  
51  
52  
53  
54  
55  
56  
57  
58  
59  
60

1  
2  
3  
4  
5 115 participated in this study. Eight patients were the same patients from our previous report  
6  
7  
8 116 [17]. Five patients had different degrees of motor dysfunction and sensory disturbances  
9  
10 117 in their upper limbs due to strokes without damage to the sensorimotor cortex, previous  
11  
12  
13 118 surgery on the motor cortex, or brain tumor on the sensorimotor cortex (Table 1). Six  
14  
15  
16 119 patients with epilepsy had no motor dysfunctions or sensory disturbances. All  
17  
18  
19 120 participants or their guardians gave written informed consent to participate in the study,  
20  
21  
22 121 which was approved by the ethics committee of Osaka University Hospital (No. 08061,  
23  
24  
25 122 No. 19257).

26  
27  
28 123  
29  
30  
31

32 **2.2. Movement tasks**  
33  
34

35 125 Experiments were performed approximately 1 week after electrode placement. The  
36  
37 126 patients performed three types of upper limb movements, selecting among grasping,  
38  
39 127 pinching, hand opening, thumb flexion, and elbow flexion [17]. We presented the  
40  
41 128 patients with three sound cues at 1-s intervals. The patients performed one of three  
42  
43 129 prespecified movements after the third sound cue. The patient selected the movement  
44  
45 130 type for each trial, so the order and number of exercises were random. The numbers of  
46  
47 131 the selected movement types are shown in Table 2. The patients were instructed to  
48  
49 132 perform the selected movement once, immediately after the third cue, and to return their

1  
2  
3  
4  
5 133 hands to the resting position, which was an immediate hand posture among the  
6  
7 134 performed movements. For the resting position, patients were instructed to relax their  
8  
9 135 hands or elbows with slightly flexed joints. Each type of movement was performed  
10  
11 136 approximately 30 to 100 times. The movement instructions were delivered using a PC  
12  
13 137 monitor controlled by ViSaGe (Cambridge Research System, Rochester, UK) placed in  
14  
15 138 front of the patients.

22  
23 139  
24  
25

26 140 Table 1. Clinical profiles  
27

| Patient no. | Age (yr)/sex | Diagnosis                | Paresis in affected limb (MMT) | Sensation in affected limb |
|-------------|--------------|--------------------------|--------------------------------|----------------------------|
| 1           | 65/M         | Ruptured spinal dAVF     | spastic (4)                    | hypoesthesia               |
| 2           | 64/M         | R thalamic hemorrhage    | spastic (4)                    | hypoesthesia               |
| 3           | 20/F         | L intractable epilepsy   | none (5)                       | normal                     |
| 4           | 34/F         | R intractable epilepsy   | none (5)                       | normal                     |
| 5           | 22/F         | R intractable epilepsy   | none (5)                       | normal                     |
| 6           | 14/M         | R intractable epilepsy   | none (5)                       | normal                     |
| 7           | 13/M         | L intractable epilepsy   | none (5)                       | normal                     |
| 8           | 33/M         | R intractable epilepsy   | slightly spastic (4)           | hypoesthesia               |
| 9           | 26/M         | L brain tumor            | none (5)                       | normal                     |
| 10          | 66/F         | R subcortical infarction | spastic (4)                    | hypoesthesia               |
| 11          | 49/M         | R putaminal hemorrhage   | slightly spastic (5-)          | hypoesthesia               |

50  
51 141 <sup>a</sup>Posttransplantation of the intercostal nerve.  
52  
53

54 142 dAVF, dural arteriovenous fistula; F, female; L, left; M, male; MMT, manual muscle  
55

56  
57 143 test; R, right.  
58  
59  
60

1  
2  
3  
4  
5 144  
6  
7  
8  
9 145 **2.3. ECoG recording and preprocessing**

10  
11 146 ECoG signals were recorded at 1 kHz by an EEG-1200 system (Nihon Koden, Tokyo,  
12  
13 Japan). The subdural electrodes were placed on the sensorimotor cortex based on  
14  
15 clinical necessity. For each patient, 15–60 electrodes were implanted. All signals were  
16  
17 subtracted by the average of the signals of all electrodes at each time point, a well-  
18  
19 known method for the calculation of a common average reference [30, 31]. An  
20  
21 epileptologist identified the channels with severe noise, and these were excluded from  
22  
23 the analysis. Three channels for patient 7 and one channel for patient 10 were removed  
24  
25 (Supplementary Figures 3, 5).

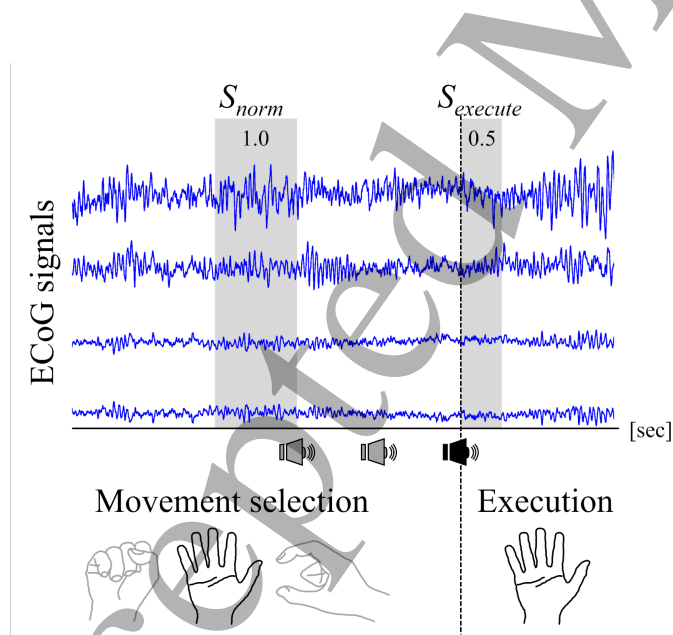
26  
27  
28  
29  
30  
31  
32 153 (Supplementary Figures 3, 5).  
33  
34  
35 154 For the following analysis, we used the ECoG signals at 0.5 s after the third sound cue,  
36  
37  
38 155  $S_{execute}$ , and at 1.0 s before the first sound cue,  $S_{norm}$  (Figure 1). Here,  $S_{execute}$  and  
39  
40 156  $S_{norm}$  were composed of  $n$  channels for 500 and 1000 time points, respectively. Here,  
41  
42  
43 157 we used 1.0 s of ECoG signals for normalization ( $S_{norm}$ ) to decrease the variability in  
44  
45  
46 158  $S_{norm}$ . Notably, we also used 0.5 s of ECoG signals before the first sound cue for the  
47  
48  
49 159  $S_{norm}$ , but the classification accuracy using the FFT feature did not significantly change  
50  
51  
52 160 with the normalization of 0.5 s (supplementary information, table 1). All processes were  
53  
54  
55 161 implemented by MATLAB (R2015b).

162

163 Table 2. Movement tasks and recording conditions

| Patient no. | Pre-specified movement tasks (label 1, 2, 3) | Trial count (label 1) | Trial count (label 2) | Trial count (label 3) | Number of electrodes |
|-------------|--|-----------------------|-----------------------|-----------------------|----------------------|
| 1           | Grasp, pinch, open                           | 42                    | 46                    | 32                    | 60                   |
| 2           | Grasp, pinch, open                           | 19                    | 25                    | 33                    | 60                   |
| 3           | Grasp, pinch, open                           | 44                    | 36                    | 37                    | 20                   |
| 4           | Grasp, pinch, open                           | 34                    | 44                    | 49                    | 30                   |
| 5           | Grasp, pinch, open                           | 42                    | 39                    | 39                    | 30                   |
| 6           | Grasp, pinch, open                           | 34                    | 20                    | 22                    | 15                   |
| 7           | Grasp, pinch, open                           | 37                    | 50                    | 36                    | 27                   |
| 8           | Rock, paper, scissors                        | 31                    | 30                    | 39                    | 49                   |
| 9           | Rock, paper, scissors                        | 20                    | 20                    | 20                    | 24                   |
| 10          | Grasp, thumb, elbow                          | 36                    | 40                    | 36                    | 20                   |
| 11          | Grasp, thumb, elbow                          | 71                    | 69                    | 39                    | 32                   |

164



165

166 Figure 1. ECoG signals during hand movements. After selecting one of the three

167 movement types, the patient performed the selected movements once after the third

1  
2  
3  
4  
5 168 sound cue (shown as black speaker). The ECoG signals during the 0.5 s before the first  
6  
7 169 sound cue and those after the last sound cue were used for the analysis.  
8  
9  
10  
11  
12  
13

14 171 **2.4. FFT features for neural decoding**  
15  
16

17 172 As a conventional approach for the neural decoding of ECoG signals, FFT was used to  
18  
19 173 create the FFT features of the signals [32]. FFT was applied as 512 points and 1024  
20  
21 174 points for  $S_{execute}$  (500 points) and  $S_{norm}$  (1000 points), respectively, by zero-  
22  
23 padding with a hamming window.  $S_{norm}$  was only used to normalize  $S_{execute}$  to  
24  
25 175 reduce variation among trials. The power features of four frequency bands were  
26  
27 176 obtained by averaging the estimated power of the four frequency bands: theta (4–8 Hz),  
28  
29 177 alpha (8–13 Hz), beta (13–30 Hz), and high gamma (80–150 Hz). In addition to these  
30  
31 178 powers, we also calculated the average 0 Hz power for  $S_{execute}$  and  $S_{norm}$ . Finally,  
32  
33 179 these five features of  $S_{execute}$  were normalized by the mean power  $\bar{p}_{norm}$  and  
34  
35 180 standard deviations  $\sigma_{norm}$  of the corresponding features derived from  $S_{norm}$  to create  
36  
37 181 the FFT features, which consisted of five features by  $n$  channels [17, 33]. The features  
38  
39 182 were obtained by  $\frac{\mathbf{p}_{execute} - \bar{\mathbf{p}}_{norm}}{\sigma_{norm}}$  ( $\mathbf{p}_{execute}$  is the power feature vector of  $S_{execute}$ ).  
40  
41 183 Here, the FFT powers of  $S_{execute}$  were normalized because normalized features were  
42  
43 184 shown to be decoded with better accuracy than FFT powers of  $S_{execute}$  without  
44  
45  
46  
47  
48  
49  
50  
51  
52  
53  
54  
55  
56  
57  
58  
59  
60

1  
2  
3  
4  
5 186 normalization [15].  
6  
7  
8  
9  
10  
11  
12  
13  
14  
15  
16  
17  
18  
19

### 188 2.5.1. Computation of the dynamic mode decomposition

189 Assuming that the sensorimotor cortex during exercise is one dynamic system, the  
190 system can be described using its observed variable  $\mathbf{x}$  (ECoG signals) as follows:

191 
$$\frac{d\mathbf{x}}{dt} = f(\mathbf{x}, t; \mu),$$

192 where  $t$  and  $\mu$  are the time and system parameters. Because the actual recorded  
193 signals are values at discrete times,  $\mathbf{x}_k = \mathbf{x}(k\Delta t)$  is delimited by  $\Delta t$ , and the dynamic  
194 system is described as  $\mathbf{x}_{k+1} = \mathbf{F}(\mathbf{x}_k)$ . Although  $\mathbf{F}$  is difficult to obtain analytically, we  
195 can obtain linearly approximated dynamics  $\mathbf{x}_{k+1} = \mathbf{A}\mathbf{x}_k$  from the recorded signals.

196 The DMD can be used to estimate  $\mathbf{A}$  of unknown dynamics.

197 First, we briefly explain how the DMD was evaluated for column vector  $\mathbf{x}_k$ , which is  
198 the observations across all electrodes at the  $k$ -th time sample [27]. Gathering  
199 measurements from  $m$  snapshots in time, we constructed two  $n \times (m - 1)$  raw data  
200 matrices,  $\mathbf{X}_1$  and  $\mathbf{X}_2$ :

201  
202 
$$\mathbf{X}_1 = [\mathbf{x}_1 \quad \mathbf{x}_2 \quad \dots \quad \mathbf{x}_{m-1}]$$

203 
$$\mathbf{X}_2 = [\mathbf{x}_2 \quad \mathbf{x}_3 \quad \dots \quad \mathbf{x}_m]$$

1  
2  
3  
4  
5  
6  
7  
2048  
9  
205 Here, the DMD of the data matrix pair  $\mathbf{X}_1$  and  $\mathbf{X}_2$  was given by the10  
11  
206 eigendecomposition of the transition matrix  $\mathbf{A}$ , which is an  $n \times n$  matrix satisfying  $\mathbf{X}_2$   
12  
13  
14  
15  
 $= \mathbf{AX}_1.$ 16  
17  
208 Using the singular value decomposition (SVD) of the data matrix  $\mathbf{X}_1 = \mathbf{U}\Sigma\mathbf{V}^*$ ,  $\mathbf{A}$   
18  
19  
209 was approximated as  $\mathbf{A} \approx \mathbf{X}_2\mathbf{X}_1^{-1} \triangleq \mathbf{X}_2\mathbf{V}\Sigma^{-1}\mathbf{U}^*$  ( $^{-1}$  is pseudoinverse matrix of  $\mathbf{X}_1$ ).  
21  
2223  
24  
210 However, the eigenvalue decomposition of  $\mathbf{A}$  requires a tremendous amount of  
25  
26 calculation. Therefore, we used the orthogonal matrix  $\mathbf{U}$  to make  $\tilde{\mathbf{A}} \triangleq \mathbf{U}^T \times \mathbf{A} \times \mathbf{U} =$   
27  
28  
211  $\mathbf{U}^T \times \mathbf{X}_2 \mathbf{V} \Sigma^{-1}$ , which has fewer dimensions than  $\mathbf{A}$ . That is, we assumed that there exists  
29  
30  
31 some low-dimensional spatial structure in  $\mathbf{X}_1$ . Using  $\tilde{\mathbf{A}}$ , the calculation for the  
32  
33  
34 eigenvalue decomposition of  $\mathbf{A}$  was reduced. The eigenvalues  $\Lambda$  of the eigenvalue  
35  
36  
37 decomposition  $\tilde{\mathbf{A}}$  were obtained by  $\tilde{\mathbf{A}}\mathbf{W} = \mathbf{W}\tilde{\Lambda}$ , with the eigenvalue matrix  $\tilde{\Lambda}$   
38  
39  
40  
41 approximately equal to the eigenvalue matrix of  $\mathbf{A}$ .  
42  
4344  
45  
217 In addition, for the exact DMD,  $\hat{\mathbf{A}} \triangleq \Sigma^{-\frac{1}{2}}\tilde{\mathbf{A}}\Sigma^{\frac{1}{2}}$  was set to obtain the eigenvector  $\mathbf{W}$   
46  
47  
218 by applying the eigenvalue decomposition  $\hat{\mathbf{A}}\mathbf{W} = \mathbf{W}\hat{\Lambda}$ . Then, by putting  $\hat{\mathbf{W}} \triangleq \Sigma^{-1}\mathbf{W}$ ,  
48  
49  
50 the DMD mode was obtained as each row of  $\hat{\Phi} \triangleq \mathbf{X}_2\mathbf{V}\Sigma^{-1} * \hat{\mathbf{W}}\hat{\Lambda}^{-1}$ .  
51  
5253  
54  
220 Here,  $\hat{\Lambda}$  is the diagonal matrix of eigenvalues  $\lambda_i$ . Each eigenvalue  $\lambda_i$  is a DMD  
55  
56 eigenvalue. Each column of  $\hat{\Phi}$  is a DMD mode  $\varphi_i$  corresponding to the eigenvalue  $\lambda_i$ .  $i$   
57  
58  
59  
60

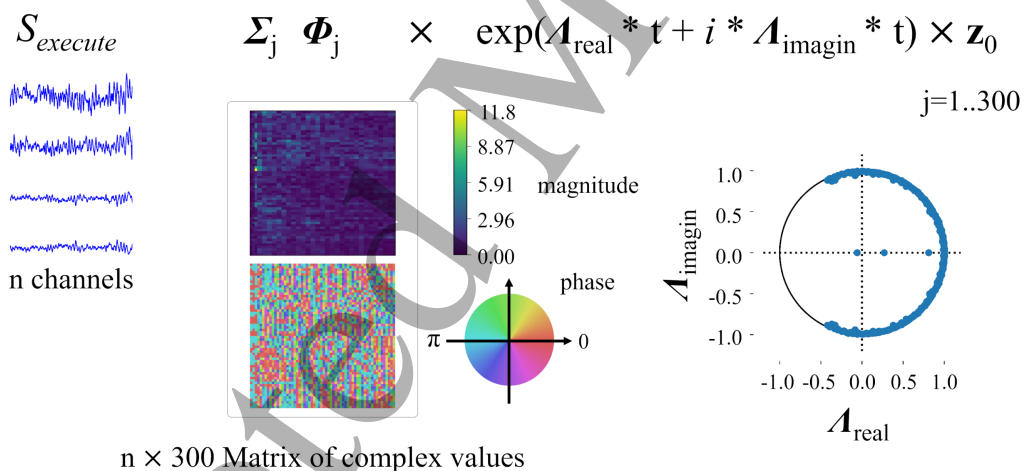
1  
2  
3  
4  
5 222 = 1, ..., m - h - 1. The absolute values and phases of  $\widehat{\Lambda}$  are the decay rates and  
6 frequencies, respectively.  
7  
8

9  
10 224 Finally, we were able to write an approximation of the observed data as a simple  
11  
12 225 dynamic model  $\widehat{X}(t)$ ,  
13  
14  
15

16  
17 226 
$$\widehat{X}(t) = \widehat{\Phi} \exp(\Omega t) z,$$
  
18  
19

20 227 where  $\Omega = \log(\Lambda)/\Delta t$ ,  $t$  is time, and  $z$  is a set of weights to match the first time point  
21  
22 228 measured such that  $\widehat{X}(1) = \widehat{\Phi}z$ . It should be noted that  $\widehat{\Phi}$  and  $\Omega$  are sets of vectors  
23  
24 229 with complex values (Figure 2).  
25  
26  
27

28 230



45  
46 231  
47  
48 232 Figure 2. DMD of ECoG signals during movements. The ECoG signals of  $n$  channels  
49  
50 233 ( $S_{execute}$ ) were converted into the  $n \times 300$  matrix of magnitude and phases that  
51  
52 234 represents the complex values of the DMD modes  $\Phi_j$ .  $\Lambda_{real}$  and  $\Lambda_{imagin}$  represent the  
53  
54 235 decay rates and frequencies.  
55  
56  
57  
58  
59  
60

1  
2  
3  
4  
5  
6  
7  
236

8       237       DMD was originally used to evaluate the  $\mathbf{X}_1$  of  $n \gg m$ . However, in our data, the  
 9  
10      238       ECoG signal has approximately 100 channels for 500 ms. Therefore, to calculate the  
 11  
12      239       DMD, we constructed a new augmented data matrix  $\mathbf{X}_{1\text{ aug}}$  as follows:

16  
17  
18  
19  
20  
21  
22  
23  
24  
25  
240

$$\mathbf{X}_{1\text{ aug}} = \begin{bmatrix} \mathbf{x}_1 & \mathbf{x}_2 & \dots & \mathbf{x}_{m-h} \\ \mathbf{x}_2 & \mathbf{x}_3 & \dots & \mathbf{x}_{m-h+1} \\ \vdots & \vdots & \vdots & \vdots \\ \mathbf{x}_h & \mathbf{x}_{h+1} & \dots & \mathbf{x}_{m-1} \end{bmatrix}$$

26       241       Here,  $h$  is a minimum integer that satisfies  $h > \frac{m+1}{n+1}$ .  $\mathbf{X}_{1\text{ aug}}$  is an array generated  
 27  
28      242       from  $\mathbf{X}_1$  of  $m$  length by stacking them in the channel dimension by sliding the step one  
 29  
30      243       by one. We constructed  $\mathbf{X}_{2\text{ aug}}$  using the same procedure.

34  
35       244       The DMD features were obtained from  $\mathbf{X}_{1\text{ aug}}$  and  $\mathbf{X}_{2\text{ aug}}$  by the method previously  
 36  
37      245       mentioned. Notably, we generated  $\mathbf{X}_{1\text{ aug}}$  and  $\mathbf{X}_{2\text{ aug}}$  using only  $S_{execute}$  without any  
 38  
39      246       normalization by  $S_{norm}$  to avoid damaging the spatial relations among the channels of  
 40  
41      247        $S_{execute}$  by subtracting the averages and dividing the standard deviations of  $S_{norm}$  for  
 42  
43      248       each channel. In fact, the DMD mode  $\hat{\Phi}$  will be changed by the normalization of  $\mathbf{X}_{1\text{ aug}}$   
 44  
45      249       and  $\mathbf{X}_{2\text{ aug}}$  by the same  $S_{norm}$ .

52  
53       250       Here, the number of channels,  $n$ , and the size of the  $\mathbf{X}_{1\text{ aug}}$  were different among the  
 54  
55      251       subjects. Therefore, to equalize the number of DMD modes, we selected the 300 modes

1  
2  
3  
4  
5 252 with the largest singular values. Because the DMD mode  $\varphi_{i \text{ aug}}$  yielded from  $X_1 \text{ aug}$  and  
6  
7 253  $X_2 \text{ aug}$  was a vector of  $hn \times 1$ , we used the first  $n$  vector of  $\varphi_{i \text{ aug}}$  corresponding to  $\varphi_i$ ,  
8  
9 254 which is the mode for the original data  $X_1$  and  $X_2$  for the decoding task. In addition,  
10  
11 255 because the size of  $\varphi_i$  generally decreases with the higher frequency range (imagery part  
12  
13 256 of the eigenvalue  $\lambda_i$ ), we normalized each mode by the L2 norm of the mode  $\varphi_i$ .  
14  
15  
16  
17 257 Notably, the principal angle requires the orthonormal matrix to be equalized among the  
18  
19 258 permutation of the composed vectors. To simplify the calculation, we aligned the mode  
20  
21 259 magnitude by the L2 norm instead of the orthogonalization.  
22  
23  
24  
25  
26  
27  
28  
29  
30  
31  
32 260  
33  
34 261 **2.5.2. Neural decoding by the Grassmann kernel**  
35  
36 262 The FFT feature is represented as a set of vectors of  $n \times 5$ . The DMD features are  
37  
38 263 composed of eigenvectors  $\Phi_j$  corresponding to a characteristic frequency  $\omega_j$  ( $j =$   
39  
40 264 1 ... 300).  
41  
42  
43  
44 265 Therefore, the DMD feature is represented as a set of vectors  $n \times 300$ . Notably, the  
45  
46  
47 266 DMD feature for classification is a subspace of the representation. To compare the  
48  
49  
50 267 subspaces for the classification task, we evaluated a principal angle, which measures the  
51  
52  
53 268 distance between the subspaces based on the set of vectors. Here, based on the principal  
54  
55  
56 269 angle, we used the Grassmann kernel to classify the set of vectors by SVM [29].  
57  
58  
59  
60



1  
2  
3  
4  
5 270  $Y_1$  and  $Y_2$  were set as two orthonormal matrices of size  $D$  by  $m$ . The principal angles  
6

7 271  $0 \leq \theta_1 \leq \dots \leq \theta_m \leq \pi/2$  between two subspaces,  $\text{span}(Y_1)$  and  $\text{span}(Y_2)$ , were defined  
8

9 272 recursively by the following:  
10  
11  
12

13 273  $\cos \theta_k = \max_{u_k \in \text{span}(Y_1)} \max_{v_k \in \text{span}(Y_2)} u_k' v_k$ , subject to  
14  
15

16 274  $u_k' u_k = 1, v_k' v_k = 1,$   
17  
18

19 275  $u_k' u_i = 0, v_k' v_i = 0, (i = 1, \dots, k-1)$   
20  
21

22 276 The principal angles were computed from the SVD of  $Y_1' Y_2$  as follows:  
23  
24

25 277  $Y_1' Y_2 = U(\cos \Theta) V'$ ,  
26  
27

28 278 where  $U = [u_1 \dots u_m]$ ,  $V = [v_1 \dots v_m]$ , and  $\cos \Theta$  is the diagonal matrix  
29  
30

31 279  $\cos \Theta = \text{diag}(\cos \theta_1 \dots \cos \theta_m).$   
32  
33

34 280 Based on the principal angles, the projection kernel of subspaces  $Y_1$  and  $Y_2$  was  
35  
36

37 281 determined as follows:  
38  
39

40 282  $k_p(Y_1, Y_2) = \|Y_1' Y_2\|_F^2 = \text{tr}[(Y_1 Y_1')(Y_2 Y_2')]$   
41  
42

43 283 Here, we applied the projection kernel to the DMD features  $\hat{\Phi}_i$  and  $\hat{\Phi}_j$  to generate the  
44  
45

46 284 Gram matrix  $k_p(\hat{\Phi}_i, \hat{\Phi}_j)$ . To apply the Gram matrix to SVM, each component of the  
47  
48

49 285 Gram matrix was divided by the average of all components of the Gram matrix. For  
50  
51

52 286 comparison, the FFT features were also classified using SVM with the projection  
53  
54

55 287 kernel. We also calculated the inner product matrix correlation [34] defined as  
56  
57

58  
59  
60

1  
2  
3  
4  
5 288  $r_{in}(\mathbf{A}, \mathbf{B}) = \frac{\text{tr}(\mathbf{A}'\mathbf{B})}{[\text{tr}(\mathbf{A}'\mathbf{A})\text{tr}(\mathbf{B}'\mathbf{B})]^{1/2}}$  of two  $i \times j$  matrices  $\mathbf{A}$  and  $\mathbf{B}$  to examine the independent  
6  
7  
8 289 information contained in the DMD and FFT features.  
9  
10  
11  
12  
13

14 291 **2.5.3. T-distributed stochastic neighbor embedding analysis of the Gram matrix**  
15  
16

17 292 Based on the Grassmann kernel, the distance between each DMD mode is represented  
18  
19 293 in the Grassmann space, in which the distance between each mode of the Gram matrix  
20  
21  
22 294  $\mathbf{G}_{i,j}$  corresponding to the inner product of  $\widehat{\Phi}_i$  and  $\widehat{\Phi}_j$  was defined as  $Distance_{i,j} =$   
23  
24  
25 295  $\sqrt{\mathbf{G}_{i,i} + \mathbf{G}_{j,j} - 2\mathbf{G}_{i,j}}$ . To visualize the distribution of each DMD mode in the space, we  
26  
27  
28 296 applied t-distributed stochastic neighbor embedding (t-SNE) to the space [35].  
29  
30  
31  
32  
33  
34

35 298 **2.6. Decoding analysis**  
36  
37

38 299 The classifier was independently trained for each patient by SVM. The classification  
39  
40 300 accuracy was evaluated by 10-fold nested cross validation. In the nested loop, the cost  
41  
42  
43 301 parameter was optimized in the range of  $10^{-1} < \text{cost} < 10^8$ . The classification  
44  
45  
46 302 accuracies were evaluated as balanced accuracy because the number of each movement  
47  
48  
49 303 type was uneven [36]. The balanced accuracy is defined as the average of recall  
50  
51  
52 304 obtained in each category.

53  
54  
55 305 We evaluated how the classification accuracies depend on the characteristic  
56  
57  
58  
59  
60

frequency. We selected 10 modes  $\Phi_j$  ( $j = 1 \dots 10$ ), which have the characteristic

frequency  $\omega_j$  closest to 29 selected frequencies: 10, 20, ..., 290 Hz. Then, the

classification was performed with 10 selected modes for each frequency.

$\Phi_j$  is the vector of complex values. Each complex value is expressed as a radius

and a phase in a complex plane. To evaluate how much the phase information

contributes to the decoding, we also evaluated the classification accuracy using the

DMD features in which the phases of each  $\Phi_j$  were randomized.

313

## 314 **2.7. Statistical tests**

315 We compared the classification accuracies evaluated by the two types of features, DMD

316 features and FFT features, by Student's paired *t*-test, with  $p < 0.05$  indicating

317 significance.

318 We also compared the correctness of prediction by SVM trained with DMD and FFT

319 features by Welch's *t*-test, with  $p < 0.05$  indicating significance.

320 The classification accuracy of each frequency was compared to the classification

321 accuracy using the same features with shuffled labels by using Bonferroni-corrected

322 Student's paired *t*-test, with  $p < 0.05$  indicating significance.

323 The phases of the DMD mode of each electrode were evaluated by the Rayleigh test

1  
2  
3  
4  
5 324 to show some biases in the phase distribution of the electrode among each movement  
6  
7 325 task.  
8  
9  
10  
11 326  
12  
13  
14 327 **3. Results**  
15  
16  
17 328 **3.1. Gram matrix based on projection kernel with DMD mode and clustering of**  
18  
19  
20 329 **dynamics**  
21  
22  
23 330 For illustrative patient 1, we calculated the projection kernel values  $G_{i,j}$ , which  
24  
25  
26 331 correspond to the inner products between each DMD mode  $\hat{\Phi}_i$  and  $\hat{\Phi}_j$ . The projection  
27  
28  
29 332 kernel values demonstrated some clusters according to the movement types (Figure 3A).  
30  
31  
32 333 Based on the projection kernel, we further calculated the distance matrix between each  
33  
34  
35 334 DMD mode, which represents the Grassmann space for the SVM classification. To  
36  
37  
38 335 visualize the Grassmann space, t-SNE was applied for the distance matrix to embed  
39  
40  
41 336 each trial into a two-dimensional space (Figure 3B). Each movement type was classified  
42  
43  
44 337 into different clusters. The Grassmann space using the projection kernel seemed to be  
45  
46  
47 338 successful at classifying the movement types.  
48  
49  
50 339  
51  
52  
53  
54  
55  
56  
57  
58  
59  
60

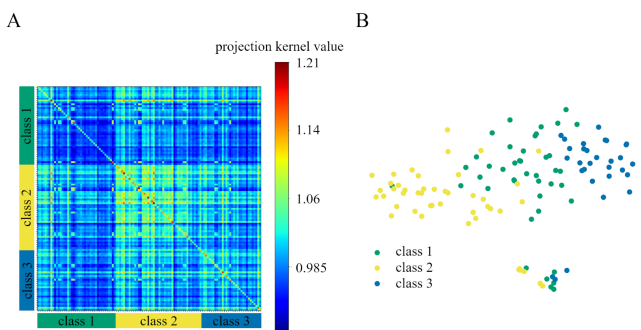


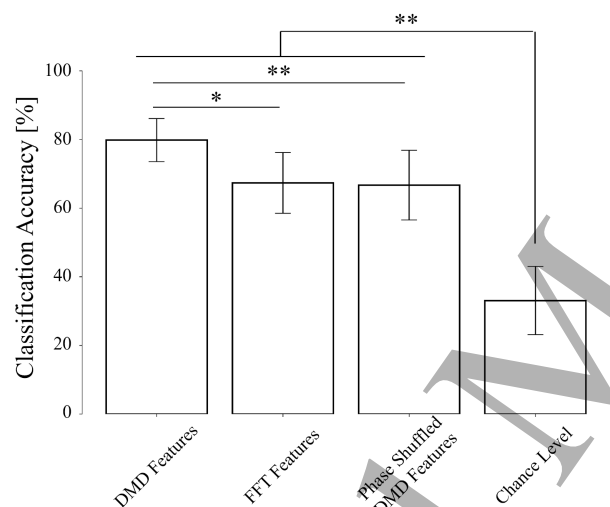
Figure 3. Gram matrix and similarity in the Grassmann space for patient 1. A. The projection kernel values were color-coded on the matrix of each trial. The numbers on the vertical and horizontal axes represent the movement type (1, grasping; 2, opening; 3, pinching). B. The distribution of the data for each trial in the Grassmann space that was embedded into two dimensions by t-SNE. Each class corresponds to the movement type.

### 3.2. Neural decoding using DMD features

Using the Grassmann kernel, the classification of the movement types was evaluated. The classification accuracy significantly varied among the different features: DMD feature, FFT feature, DMD feature with shuffled phase, and DMD features with shuffled labels ( $p = 9.12 \times 10^{-11}$ , one-way ANOVA; Figure 4). The three types of hand movements were successfully classified using the DMD features ( $79.8 \pm 6.28\%$ ; mean  $\pm$  95% confidence interval), the FFT features ( $67.3 \pm 8.56\%$ ), and the DMD features with

shuffled phase ( $66.7 \pm 9.96\%$ ), with accuracies exceeding the accuracy using the DMD features with shuffled labels ( $33.1 \pm 3.90\%$ , i.e., chance level). Among these classification schemes, the classification accuracy using the DMD features was significantly superior to that using the FFT features and the DMD features with shuffled phase ( $p < 0.05$ , paired Student's  $t$ -test, uncorrected).

360



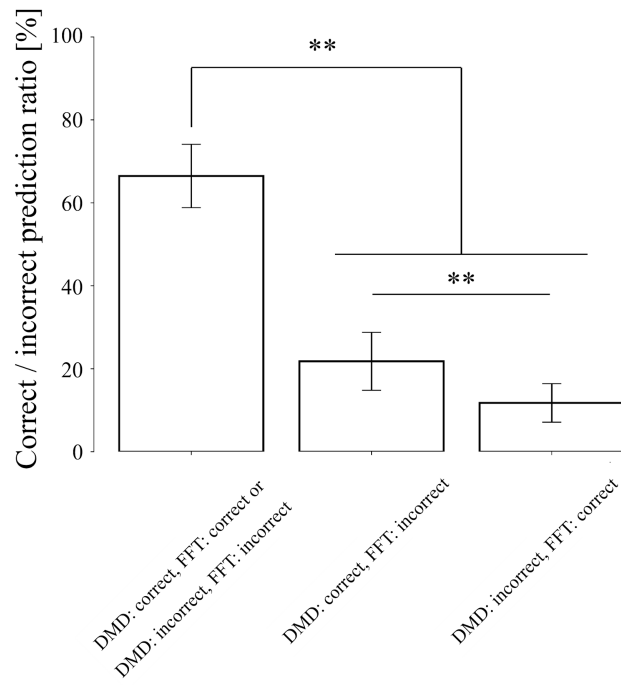
361  
362 Figure 4. Classification accuracy using different features. The mean and 95%  
363 confidence interval of the classification accuracies are shown for the classification using  
364 the DMD features, FFT features, DMD features with shuffled phase, and DMD features  
365 with shuffled labels (\* $p < 0.05$ , \*\* $p < 0.01$ , paired Student's  $t$ -test).

366  
367 We also examined how the prediction of the DMD and FFT features were correlated.

1  
2  
3  
4  
5 368 First, we evaluated the inner product matrix correlation of the Gram matrices of the DMD  
6  
7 369 features and the FFT features. For 10 out of 11 patients, the correlation was more than  
8  
9 370 0.8 (supplementary information, table 2), suggesting that the Gram matrices were similar  
10  
11 371 to each other. However, for patient 5, whose correlation was 0.359, the classification  
12  
13 372 accuracy was higher with the DMD features for this patient. Second, we compared the  
14  
15 373 predictions using two features. We divided the classification results with the two features  
16  
17 374 into three groups for each patient: Group 1, the predictions of both features were the same;  
18  
19 375 Group 2, the prediction of DMD was correct, but that of FFT was incorrect; and Group 3,  
20  
21 376 the prediction of DMD was incorrect, but that of FFT was correct. Among all patients,  
22  
23 377 the ratio of the groups was significantly high for Group 1 ( $66.5 \pm 8.02\%$ ) (Figure 5).  
24  
25 378 Moreover, for the conflicting predictions, Group 2 was significantly larger than Group 3.  
26  
27 379 Therefore, these two features mostly result in the same predictions, but in the case of  
28  
29 380 conflicting predictions, the DMD features predicted significantly better than the FFT  
30  
31 381 features.

382

1  
2  
3  
4  
5  
6  
7  
8  
9  
10  
11  
12  
13  
14  
15  
16  
17  
18  
19  
20  
21  
22  
23  
24  
25  
26  
27  
28  
29  
30  
31  
32  
33  
34  
35  
36  
37  
38  
39  
40  
41  
42  
43  
44  
45  
46  
47  
48  
49  
50  
51  
52  
53  
54  
55  
56  
57  
58  
59  
60



383

384 Figure 5. Comparison of correctness of prediction by SVM trained with DMD and FFT

385 features. The mean and 95% confidence interval of prediction ratio where the two sets

386 of features had the same prediction label, where DMD had correct prediction labels and

387 FFT had incorrect prediction labels, and where DMD had incorrect prediction labels and

388 FFT had correct prediction labels (\*\* $p < 0.01$ , Bonferroni-corrected Welch's  $t$ -test).

389

390 We compared the classification accuracy using subsets of the DMD features to

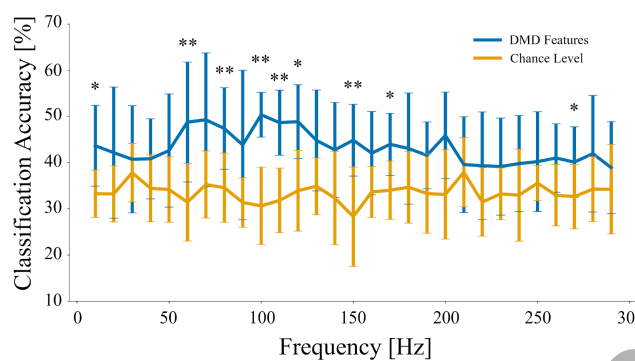
391 evaluate which frequency band modes contributed to the classification. The

392 classification accuracies using DMD features of the characteristic frequency close to the

393 selected frequency significantly exceeded the accuracy by chance at 60, 80, 100, 110,

1  
2  
3  
4  
5 394 and 150 Hz ( $p < 0.01$ , Bonferroni-corrected paired Student's  $t$ -test; Figure 6). The peak  
6  
7 395 mean accuracy was  $50.4 \pm 2.42\%$  (mean  $\pm$  95% confidence interval) at 100 Hz, which  
8  
9 396 corresponds to the high gamma band.

10  
11 397

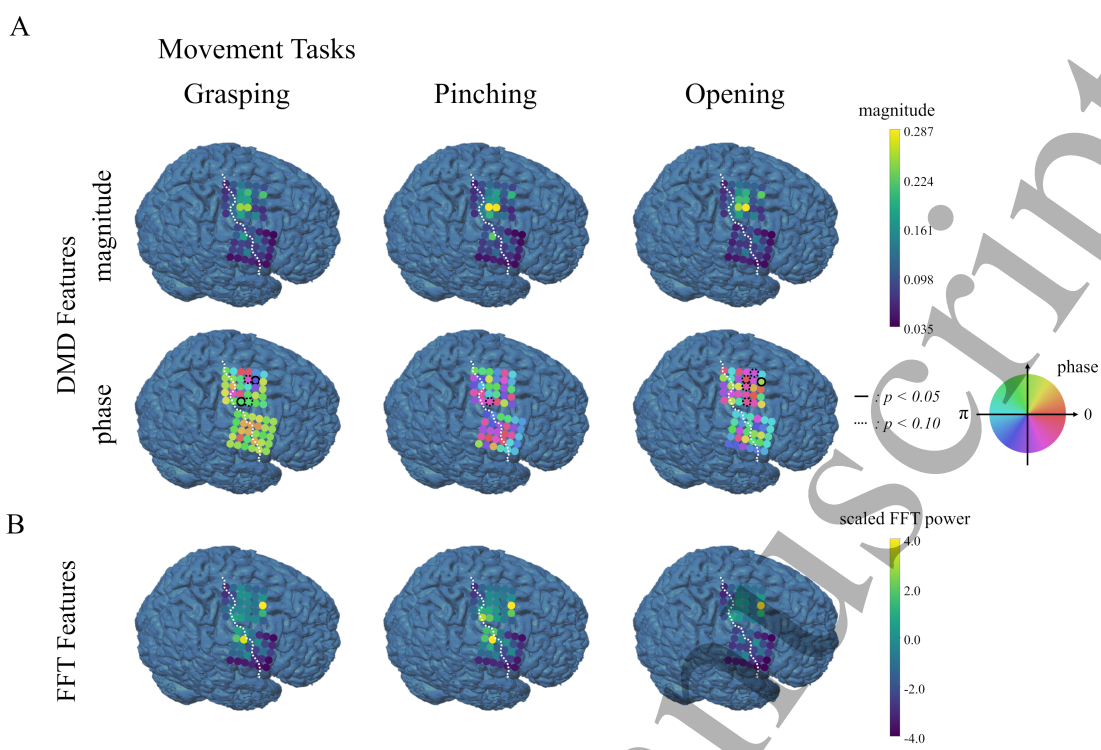


12  
13 398  
14  
15 399 Figure 6. Classification accuracy for each frequency mode. The classification accuracies  
16  
17 400 using the DMD features whose frequency components were close to each frequency  
18  
19 401 point (blue line) were compared to those using the same features with shuffled labels  
20  
21 402 (chance level, orange line). The accuracies at approximately 100 Hz were significantly  
22  
23 403 higher than those at chance level ( $*p < 0.05$ ,  $**p < 0.01$ , paired Student's  $t$ -test,  
24  
25 404 Bonferroni corrected).

26  
27 405  
28  
29 406 **3.3. DMD modes during movement**

30  
31 407 The DMD mode captured spatiotemporal patterns characterizing movement type. For  
32  
33 408 the high gamma band frequency (80–150 Hz) in patient 1, the averaged amplitudes and

1  
2  
3  
4  
5 409 phases of the DMD mode were evaluated and color-coded according to electrode  
6  
7 410 position (Figure 7A). The magnitude of the DMD mode was high at the electrodes on  
8  
9 411 the primary motor cortex and demonstrated different patterns in accordance with  
10  
11 412 movement type for patient 1. In addition, the relative phases of each electrode were  
12  
13 413 significantly biased around the motor cortex, and the averaged relative phases were  
14  
15 414 different among movement types. Similarly, the magnitudes and phases of the DMD  
16  
17 415 modes changed based on the movement types for all other patients (supplementary  
18  
19 416 information). On the other hand, although the FFT powers of each electrode averaged  
20  
21 417 among the same frequency band demonstrated some spatial pattern characterizing the  
22  
23 418 movement type, the distribution of the high powers was different than that of the  
24  
25 419 magnitude of the DMD mode and not restricted around the primary motor cortex  
26  
27 420 (Figure 7B). The DMD mode captured some characteristic spatiotemporal patterns of  
28  
29 421 the phases and magnitudes.  
30  
31  
32  
33  
34  
35  
36  
37  
38  
39  
40  
41  
42  
43  
44  
45  
46  
47  
48  
49  
50  
51  
52  
53  
54  
55  
56  
57  
58  
59  
60



424 Figure 7. DMD features and FFT features for patient 1. A. The top row represents the  
 425 averaged magnitudes of the DMD modes at each electrode. These magnitudes were  
 426 obtained by averaging the mode magnitudes in the high gamma band among each  
 427 movement type. The bottom row represents the averaged phases of the DMD modes.  
 428 The phase was evaluated for the modes with positive imagery components. Notably,  
 429 each DMD mode was composed of a pair of complex conjugates. The phase of each  
 430 electrode was subtracted by the phase of electrode number 1 (upper right of 60  
 431 displayed electrodes). The relative phases were averaged among each movement type.  
 432 The relative phases at the electrodes with black circles were significantly biased ( $p <$   
 433 0.05, uncorrected Rayleigh test). The white dotted line represents the location of the

1  
2  
3  
4  
5 434 central sulcus. B. The scaled FFT power was averaged between 80 and 150 Hz (high  
6  
7 gamma band) of each movement type and color coded by electrode position.  
8  
9  
10  
11  
12  
13  
14 436  
15  
16  
17 437 **4. Discussion**  
18  
19  
20 438 Our analyses indicated that the DMD mode with projection kernel provided better  
21  
22 accuracy of the neural decoding than the FFT power, thereby demonstrating that DMD  
23  
24 succeeded in capturing neural information better than FFT. Moreover, the projection  
25  
26 kernel was suggested to represent the characteristic differences in ECoG signals among  
27  
28 different movement types. Our proposed method using DMD with a projection kernel is  
29  
30  
31 441 a promising technique for neural decoding.  
32  
33  
34  
35 442 DMD succeeded in extracting some spatial and temporal patterns characterizing  
36  
37  
38 443 three types of hand movements. Although a previous study demonstrated that DMD  
39  
40 extracts some characteristic spatial patterns in ECoG signals [27], it remained unclear  
41  
42 whether these patterns included more information about the movement types than the  
43  
44 patterns evaluated by FFT. In our study, the decoding accuracy using DMD features was  
45  
46  
47 448 higher than that using FFT and DMD features with shuffled phases. Notably, both DMD  
48  
49 and FFT were able to capture spatial and temporal patterns of each frequency range, as  
50  
51  
52 450 illustrated in Figure 4. However, FFT was not able to maintain the information of  
53  
54  
55  
56  
57  
58  
59  
60

1  
2  
3  
4  
5 452 phases between the dynamics of different channels. Indeed, the classification accuracy  
6  
7 453 using the DMD mode significantly decreased when the phases of the DMD modes were  
8  
9 454 shuffled and were similar to the accuracy using the FFT. Moreover, comparing the  
10  
11 455 predictions of the DMD features and the FFT features, these predictions mostly  
12  
13 456 overlapped, but the DMD features had more useful information than the FFT features.  
14  
15  
16  
17  
18 457 Therefore, our data suggest that the DMD mode improved the classification accuracy  
19  
20  
21 458 compared to the FFT by capturing some spatially and temporally coherent patterns in  
22  
23  
24 459 the ECoG signals to obtain motor information.

25  
26  
27  
28  
29 460 Among the frequency features examined, the DMD modes at approximately 100 Hz  
30  
31 461 demonstrated higher classification accuracy, implying that they contained a larger  
32  
33 462 amount of motor information. Some studies using FFT powers have also shown that the  
34  
35 463 frequency powers at approximately 100 Hz provide more motor information [15, 37].  
36  
37  
38  
39 464 Here, DMD was suggested to extract the spatial and temporal pattern relating to the  
40  
41 465 oscillation at 100 Hz. Moreover, our results demonstrated that the DMD mode close to  
42  
43 466 60 Hz was also decoded with accuracy exceeding the chance level. Although a previous  
44  
45 467 study using FFT signals demonstrated that the powers at approximately 60 Hz were  
46  
47 468 difficult to decode due to some electrical power noise [37], our results suggested that  
48  
49 469 the DMD mode is useful for extracting neural information from the ECoG signals, even  
50  
51  
52  
53  
54  
55  
56  
57  
58  
59  
60

1  
2  
3  
4  
5 470 with noise.  
6  
7  
8 471 There are some problems in applying the proposed decoding method to a BCI. First,  
9  
10 472 the DMD mode calculation must be made within at least several hundred milliseconds,  
11  
12  
13 473 which would require sufficient machine power and an appropriate approximation of the  
14  
15  
16 474 calculation. An incremental SVD might be useful to obtain such an appropriate  
17  
18  
19 475 approximation [38-40]. Second, we might need to select an appropriate DMD mode for  
20  
21  
22 476 online use during which the activity patterns of the brain continuously change. Because  
23  
24  
25 477 DMD assumes a stationary nonlinear property over a certain period of time, even for  
26  
27  
28 478 nonstationary dynamics, adapting the method to nonstationary data might be difficult.  
29  
30  
31 479 Therefore, some other machine learning techniques, such as a hidden Markov model,  
32  
33  
34 480 may be needed to address nonstationary states [41].  
35  
36  
37  
38 481 Although some technical improvements (e.g., calculation speed, adapting to  
39  
40  
41 482 nonstationary data) are necessary, improvements in the decoding accuracy of the  
42  
43  
44 483 performed movement types will improve the BCI as a communication device for the  
45  
46  
47 484 patient with limited ability to move their bodies. Our previous study demonstrated that  
48  
49  
50 485 the ECoG signals between the performed movement and attempted movements of  
51  
52  
53 486 paralyzed patients were similar and were decoded similarly. Our proposed method is  
54  
55  
56 487 also expected to improve the performance of attempted movements. Therefore, our  
57  
58  
59  
60

1  
2  
3  
4  
5 488 proposed method with DMD will improve the decoding accuracy for paralyzed patients.  
6  
7  
8 489 Using precise decoding of attempted movements, paralyzed patients will be able to  
9  
10 490 control some external devices to communicate with others [10]. Our method will  
11  
12  
13 491 improve BCI performance to realize better communication using BCI for paralyzed  
14  
15  
16 492 patients.

17  
18  
19 493 Practically, our method can be applied for to the functional mapping of movements  
20  
21  
22 494 or other various cortical functions, such as language, which has been developed with  
23  
24  
25 495 power spectral analysis of ECoG signals [42]. DMD will reveal the spatially and  
26  
27  
28 496 temporally coherent pattern of the ECoG signals in the characteristic frequency range  
29  
30  
31 497 with the highest information regarding particular cortical functions and might improve  
32  
33  
34 498 the accuracy of the functional mapping compared to that using power spectral analysis  
35  
36  
37 499 without phase coherence among electrodes. Similarly, our method can be applied to  
38  
39  
40 500 identify particular characteristic ECoG signals related to epileptic activity. Our neural  
41  
42  
43 501 decoding with DMD will be useful to identify spatially and temporally coherent patterns  
44  
45  
46 502 that represent particular types of information.

47  
48  
49 503 This study had some limitations. To simplify and shorten the calculation, we  
50  
51  
52 504 aligned the mode magnitude by the L2 norm instead of the orthogonalization. Therefore,  
53  
54  
55 505 the projection kernels between two matrices were not guaranteed to be the same when

1  
2  
3  
4  
5 506 the rows of the matrix were exchanged with each other [29]. However, our results  
6  
7 507 demonstrated that the simplified method succeeded in decoding three movement types  
8  
9 508 with accuracy that exceeded that using FFT. The proposed method with a projection  
10  
11 509 kernel was shown to be useful for motor decoding. Our future work should evaluate  
12  
13  
14 510 how orthogonalization affects the decoding accuracy. In addition, our current method  
15  
16  
17 511 ignored the frequency information. Although we used the DMD modes at specific  
18  
19  
20 512 frequencies, we did not use the frequency components for the decoding. The decoding  
21  
22  
23 513 accuracy is expected to improve with the addition of the frequency components into the  
24  
25  
26 514 DMD features. Notably, we compared the classification accuracy of three types of  
27  
28  
29 515 movements that were different among patients. The differences in the movement types  
30  
31  
32 516 might have affected the accuracy. However, by comparing the accuracy using FFT  
33  
34  
35 517 features and the DMD features with Grassmann kernels for each patient, we eliminated  
36  
37  
38 518 the effects of the different sets of movement types. Moreover, the ECoG signals in this  
39  
40  
41 519 study came from two types of patients with and without paralysis in their hands. These  
42  
43  
44 520 patients had different diseases and were implanted with different numbers of electrodes  
45  
46  
47 521 but implantations on their sensorimotor cortices was common among the patients.  
48  
49  
50 522 Notably, those differences induced no apparent differences in the decoding accuracies  
51  
52  
53 523 (supplementary information). However, the anatomical pattern of the DMD features

1  
2  
3  
4  
5 524 might be affected by ischemic stroke and brain tumors in the motor cortex. We have  
6  
7 525 demonstrated that the classification accuracy was significantly improved by DMD  
8  
9 526 features compared to FFT features using the same classification method for the ECoG  
10  
11 527 signals from the sensorimotor cortex in various conditions.  
12  
13  
14  
15  
16  
17 528  
18  
19  
20 529 **5. Conclusions**  
21  
22  
23 530 We demonstrated that DMD, which extracts spatial and temporal patterns with phase  
24  
25  
26 531 relations, is useful for extracting more motor information than FFT. The proposed  
27  
28  
29 532 method will be applied to improve BCIs and to capture some characteristic patterns of  
30  
31  
32 533 cortical activities related to motor functions.  
33  
34  
35  
36  
37  
38  
39  
40  
41  
42  
43  
44  
45  
46  
47  
48  
49  
50  
51  
52  
53  
54  
55  
56  
57  
58  
59  
60

536 **References**

- 537 1. Wolpaw, J.R., et al., *Brain-computer interfaces for communication and control*.  
538 Clin Neurophysiol, 2002. **113**(6): p. 767-91.
- 539 2. Kageyama, Y., et al., *Severely affected ALS patients have broad and high*  
540 *expectations for brain-machine interfaces*. Amyotroph Lateral Scler  
541 Frontotemporal Degener, 2014: p. 1-7.
- 542 3. Leuthardt, E.C., et al., *A brain-computer interface using electrocorticographic*  
543 *signals in humans*. Journal of neural engineering, 2004. **1**: p. 63-71.
- 544 4. Hochberg, L.R., et al., *Reach and grasp by people with tetraplegia using a*  
545 *neurally controlled robotic arm*. Nature, 2012. **485**(7398): p. 372-5.
- 546 5. Pandarinath, C., et al., *Neural population dynamics in human motor cortex during*  
547 *movements in people with ALS*. Elife, 2015. **4**: p. e07436.
- 548 6. Anumanchipalli, G.K., J. Chartier, and E.F. Chang, *Speech synthesis from neural*  
549 *decoding of spoken sentences*. Nature, 2019. **568**(7753): p. 493-498.
- 550 7. Chao, Z.C., Y. Nagasaka, and N. Fujii, *Long-term asynchronous decoding of arm*  
551 *motion using electrocorticographic signals in monkeys*. Front Neuroengineering,  
552 2010. **3**: p. 3.
- 553 8. Fernandez, E., et al., *Acute human brain responses to intracortical microelectrode*

- 1  
2  
3  
4  
5 554        arrays: challenges and future prospects. *Front Neuroeng*, 2014. **7**: p. 24.  
6  
7 555    9. Morris, S., et al., *Patient-specific cortical electrodes for sulcal and gyral*  
8  
9 556        *implantation*. *IEEE Trans Biomed Eng*, 2015. **62**(4): p. 1034-41.  
10  
11  
12 557    10. Vansteensel, M.J., et al., *Fully Implanted Brain-Computer Interface in a Locked-*  
13  
14  
15 558        *In Patient with ALS*. *N Engl J Med*, 2016. **375**(21): p. 2060-2066.  
16  
17  
18 559    11. Pandarinath, C., et al., *High performance communication by people with paralysis*  
19  
20  
21 560        *using an intracortical brain-computer interface*. *Elife*, 2017. **6**.  
22  
23  
24 561    12. Miller, K.J., et al., *Decoupling the cortical power spectrum reveals real-time*  
25  
26  
27 562        *representation of individual finger movements in humans*. *J Neurosci*, 2009.  
28  
29  
30 563        **29**(10): p. 3132-7.  
31  
32  
33 564    13. Flamary, R. and A. Rakotomamonjy, *Decoding Finger Movements from ECoG*  
34  
35  
36 565        *Signals Using Switching Linear Models*. *Front Neurosci*, 2012. **6**: p. 29.  
37  
38  
39 566    14. Freudenburg, Z.V., et al., *Sensorimotor ECoG Signal Features for BCI Control: A*  
40  
41  
42 567        *Comparison Between People With Locked-In Syndrome and Able-Bodied Controls*.  
43  
44  
45 568        *Front Neurosci*, 2019. **13**: p. 1058.  
46  
47  
48 569    15. Yanagisawa, T., et al., *Real-time control of a prosthetic hand using human*  
49  
50  
51 570        *electrocorticography signals*. *J Neurosurg*, 2011. **114**(6): p. 1715-22.  
52  
53  
54 571    16. Yanagisawa, T., et al., *Neural decoding using gyral and intrasulcal*

- 1  
2  
3  
4  
5 572       *electrocorticograms*. Neuroimage, 2009. **45**(4): p. 1099-106.  
6  
7 573 17. Yanagisawa, T., et al., *Electrocorticographic control of a prosthetic arm in*  
8  
9 574       *paralyzed patients*. Ann Neurol, 2012. **71**(3): p. 353-61.  
10  
11  
12  
13 575 18. Miller, K.J., *A library of human electrocorticographic data and analyses*. Nat  
14  
15  
16  
17 576       Hum Behav, 2019.  
18  
19  
20 577 19. Wang, W., et al., *An electrocorticographic brain interface in an individual with*  
21  
22  
23 578       *tetraplegia*. PLoS ONE, 2013. **8**(2): p. e55344.  
24  
25  
26 579 20. Volkova, K., et al., *Decoding Movement From Electrocorticographic Activity: A*  
27  
28  
29 580       *Review*. Front Neuroinform, 2019. **13**: p. 74.  
30  
31  
32 581 21. Rowley, C.W., et al., *Spectral analysis of nonlinear flows*. Journal of Fluid  
33  
34  
35 582       Mechanics, 2009. **641**: p. 115-127.  
36  
37  
38 583 22. Schmid, P., *Dynamic mode decomposition of numerical and experimental data*.  
39  
40  
41 584       Journal of Fluid Mechanics, 2010. **656**: p. 5-28.  
42  
43  
44 585 23. Mezic, I., *Analysis of Fluid Flows via Spectral Properties of the Koopman*  
45  
46  
47 586       *Operator*. Annual Review of Fluid Mechanics, Vol 45, 2013. **45**: p. 357-378.  
48  
49  
50 587 24. Sarkar, S., et al., *Mixed convective flow stability of nanofluids past a square*  
51  
52  
53 588       *cylinder by dynamic mode decomposition*. International Journal of Heat and Fluid  
54  
55  
56 589       Flow, 2013. **44**: p. 624-634.  
57  
58  
59  
60

- 1  
2  
3  
4  
5 590 25. Casorso, J., et al., *Dynamic mode decomposition of resting-state and task fMRI*.  
6  
7 591 Neuroimage, 2019. **194**: p. 42-54.  
8  
9  
10 592 26. Berger, E., et al., *Estimation of perturbations in robotic behavior using dynamic*  
11  
12  
13 593 *mode decomposition*. Advanced Robotics, 2015. **29**(5): p. 331-343.  
14  
15  
16  
17 594 27. Brunton, B.W., et al., *Extracting spatial-temporal coherent patterns in large-scale*  
18  
19  
20 595 *neural recordings using dynamic mode decomposition*. J Neurosci Methods, 2016.  
21  
22  
23 596 **258**: p. 1-15.  
24  
25  
26 597 28. Kutz, J.N., X. Fu, and S.L. Brunton, *Multiresolution Dynamic Mode*  
27  
28  
29 598 *Decomposition*. Siam Journal on Applied Dynamical Systems, 2016. **15**(2): p.  
30  
31  
32 599 713-735.  
33  
34  
35 600 29. Hamm, J. and D.D. Lee, *Grassmann Discriminant Analysis: a Unifying View on*  
36  
37  
38 601 *Subspace-Based Learning*. Proceedings of the 25th International Conference on  
39  
40  
41 602 Machine Learning (ICML 2008), 2008.  
42  
43  
44 603 30. Kubanek, J., et al., *Decoding flexion of individual fingers using*  
45  
46  
47 604 *electrocorticographic signals in humans*. J Neural Eng, 2009. **6**(6): p. 066001.  
48  
49  
50 605 31. Reddy, C.G., et al., *Decoding movement-related cortical potentials from*  
51  
52  
53 606 *electrocorticography*. Neurosurg Focus, 2009. **27**(1): p. E11.  
54  
55  
56 607 32. Gunduz, A., et al., *Decoding covert spatial attention using electrocorticographic*

- 1  
2  
3  
4  
5 608           *(ECoG) signals in humans.* Neuroimage, 2012. **60**(4): p. 2285-93.  
6  
7 609   33. Thomas, T.M., et al., *Decoding Native Cortical Representations for Flexion and*  
8  
9 610           *Extension at Upper Limb Joints Using Electrocorticography.* IEEE Trans Neural  
10  
11 611           Syst Rehabil Eng, 2019. **27**(2): p. 293-303.  
12  
13  
14 612   34. Ramsay, J.O., J.M.F. Tenberge, and G.P.H. Styan, *Matrix Correlation.*  
15  
16  
17 613           Psychometrika, 1984. **49**(3): p. 403-423.  
18  
19  
20 614   35. van der Maaten, L. and G. Hinton, *Visualizing Data using t-SNE.* Journal of  
21  
22  
23 615           Machine Learning Research, 2008. **9**: p. 2579-2605.  
24  
25  
26 616   36. Brodersen, K.H., et al., *The balanced accuracy and its posterior distribution.*  
27  
28  
29 617           International Conference on Pattern Recognition, 2010: p. 3121-3124.  
30  
31  
32 618   37. Pistohl, T., et al., *Decoding natural grasp types from human ECoG.* Neuroimage,  
33  
34  
35 619           2012. **59**(1): p. 248-60.  
36  
37  
38 620   38. Brand, M., *Incremental singular value decomposition of uncertain data with*  
39  
40  
41 621           *missing values.* Computer Vison - Eccv 2002, Pt 1, 2002. **2350**: p. 707-720.  
42  
43  
44 622   39. Ghashami, M., et al., *Frequent Directions: Simple and Deterministic Matrix*  
45  
46  
47 623           *Sketching.* Siam Journal on Computing, 2016. **45**(5): p. 1762-1792.  
48  
49  
50 624   40. Zhou, X., et al., *SVD-based incremental approaches for recommender systems.*  
51  
52  
53 625           Journal of Computer and System Sciences, 2015. **81**(4): p. 717-733.  
54  
55  
56  
57  
58  
59  
60

1  
2  
3  
4  
5 626 41. Wissel, T., et al., *Hidden Markov model and support vector machine based*  
6  
7 627 *decoding of finger movements using electrocorticography*. J Neural Eng, 2013.

8 628 **10(5): p. 056020.**

9  
10 629 42. Crone, N.E., A. Sinai, and A. Korzeniewska, *High-frequency gamma oscillations*  
11  
12 630 *and human brain mapping with electrocorticography*. Prog Brain Res, 2006. **159**:  
13  
14 631 p. 275-95.

15 632

16 633

17  
18 634 **Data/code availability:** The data that support the findings of this study are not  
19  
20 publicly available because they contain information that could compromise research  
21  
22 participants' privacy and/or consent. The code used in this study are publicly available  
23  
24 at <https://github.com/yanagisawa-lab>.

25 638

26  
27 639 **Declaration of interests:** We declare no competing interests.

28 640

29  
30 641 **Author contributions:** **Yoshiyuki Shiraishi:** Software, Validation, Formal analysis,  
31  
32 Investigation, Visualization, Writing-Original Draft, Writing-Review and Editing.

33  
34 643 **Yoshinobu Kawahara:** Conceptualization, Methodology, Writing-Review and Editing.

1  
2  
3  
4  
5 644 **Okito Yamashita:** Conceptualization, Writing-Review and Editing. **Ryohei Fukuma:**

6  
7 645 Software, Writing-Review and Editing. **Shota Yamamoto:** Data Curation. **Youichi**

8  
9 646 **Saitoh:** Resources. **Haruhiko Kishima:** Resources. **Takufumi Yanagisawa:**

10  
11 647 Conceptualization, Investigation, Data Curation, Writing-Original Draft, Writing-

12  
13 648 Review and Editing, Supervision, Project administration, Funding acquisition.

14  
15 649

16  
17 23 650 **Study funding:**

18  
19 26 651 This research was conducted under the Japan Science and Technology Agency (JST)

20  
21 29 652 Core Research for Evolutional Science and Technology (JPMJCR18A5). This research

22  
23 32 653 was also supported in part by the Japan Science and Technology Agency (JST)

24  
25 35 654 Precursory Research for Embryonic Science and Technology (JPMJPR1506),

26  
27 38 655 Exploratory Research for Advanced Technology (JPMJER1801) and CREST

28  
29 41 656 (JPMJCR1913); Grants-in-Aid for Scientific Research from KAKENHI (JP17H06032,

30  
31 44 657 JP15H05710 and JP18H03287); Grants from the Japan Agency for Medical Research

32  
33 47 658 and Development (AMED) (19dm0207070h0001, JP19dm0307103, JP19de0107001

34  
35 50 659 and JP19dm0307009); Contract research with the National Institute of Information and

36  
37 53 660 Communications Technology (grant #209); SIP (Innovative AI Hospital System) of

38  
39 56 661 NIBIOHN; and the Canon Foundation.

A  
c  
c  
e  
p  
t  
e  
d  
M  
a  
n  
u  
s  
c  
r  
i  
p  
t  
t  
A  
c  
c  
e  
p  
t  
e  
d  
M  
a  
n  
u  
s  
c  
r  
i  
p  
t  
t

42

662

Accepted Manuscript

1  
2  
3  
4  
5  
6  
7  
8  
9  
10  
11  
12  
13  
14  
15  
16  
17  
18  
19  
20  
21  
22  
23  
24  
25  
26  
27  
28  
29  
30  
31  
32  
33  
34  
35  
36  
37  
38  
39  
40  
41  
42  
43  
44  
45  
46  
47  
48  
49  
50  
51  
52  
53  
54  
55  
56  
57  
58  
59  
60